

Independent Control of Multiple Magnetic Microrobots in Three Dimensions

Eric Diller, Joshua Giltinan, and Metin Sitti

Abstract

A major challenge for untethered micro-scale mobile robotics is the control of many agents in the same workspace for distributed operation. In this work, we present a new method to independently control multiple sub-mm microrobots in three dimensions (3D) using magnetic gradient pulling as the 3D motion generation method. Motion differentiation is accomplished through the use of geometrically or magnetically distinct microrobots which assume different magnetization directions in a rotating or oscillating magnetic field. This allows for different magnetic forces to be exerted on each, enabling independent motion control and path following of multiple microrobots along arbitrary 3D trajectories. Path following in 3D with less than $310\ \mu\text{m}$ mean error is shown for a set of two microrobots of size $350\ \mu\text{m}$ and $1500\ \mu\text{m}$, and independent motions are shown with three microrobots. It is also shown that control of more microrobots could be possible using improved magnetic coil hardware. Microrobot diversity is analyzed with regards to the effect on independent control. The proposed addressability method could be used for the 3D control of a team of microrobots inside microfluidic channels or in the human body for localized therapy or diagnostics.

1 Introduction

Recent advances in microrobots at the sub-millimeter scale have brought new approaches to power delivery and control at the micro-scale. The current designs in literature, including electrostatic (Donald et al., 2008; Sakar et al., 2011), electromagnetic (Frutiger et al., 2009; Ghosh and Fischer, 2009; Pawashe et al., 2009b; Zhang et al., 2009a), optical (Maruyama et al., 2009), thermal (Sul et al., 2006), chemical (Solovev et al., 2009), and bacteria propelled systems (Behkam and Sitti, 2007; Martel et al., 2009; Sitti, 2009), have demonstrated wireless motion control of individual mobile microrobots. It is difficult to control multiple microrobots with these microrobotic systems because driving signals are typically uniform in the workspace, so all agents receive identical control inputs. Thus, such systems are highly underactuated and without onboard circuitry and actuators to decode selective control signals, mechanical selection methods must be developed for the full control of multiple microrobots. Independent control of multiple microrobots could be useful for tasks in microfluidics, microfactories or in healthcare where high throughput or distributed operation is an advantage. As microrobots are typically made using bulk fabrication techniques and are

E. Diller and J. Giltinan are with the Department of Mechanical Engineering, Carnegie Mellon University, Pittsburgh, PA 15213, USA [ediller, jgiltina}@andrew.cmu.edu

M. Sitti is with the Department of Mechanical Engineering and the Robotics Institute, Carnegie Mellon University, Pittsburgh, PA 15213, USA sitti@cmu.edu

designed to fit into small confined areas, they are well suited to operate in teams for increased speed and capability. For example, teams could be useful when microrobots each have a different function such that the desired microrobot can be brought to the target area at the appropriate time. Multi-robot control could also be useful for executing parallel payload delivery or remote interventions in liquid regions of the body, such as in the eye, urinary tract, cardiovascular system or the cerebral-spinal fluid (Nelson et al., 2010).

Previously, researchers have shown the coupled control of multiple microrobots through the use of specialized addressing surfaces or through differing dynamic responses of heterogeneous microrobot designs, all in two dimensions on a flat operating surface. Control of multiple microrobots operating on a two dimensional (2D) planar surface has been achieved in mainly two ways: Localized selective trapping and through the use of heterogeneous microrobot designs. In localized trapping, embedded electrodes or magnets are used to only retard the motion of a single agent. This retarding force is created by localized electrostatic (Pawashe et al., 2009a) or magnetic (Diller et al., 2011b) fields, and is capable of completely independent (noncoupled) control of multiple agents, at the cost of using embedded electrodes or magnets at a distance comparable to the desired spatial resolution of the addressing. In addressing through heterogeneous microrobot designs, the agents are designed to each respond differently to the same input signals. To achieve independent responses, where microrobot motions are not linearly related to one another, some type of dynamic response is required. In Donald et al. (2008), different critical turning voltages are used to independently steer up to four electrostatically-actuated microrobots. Using appropriate control algorithms, independent positioning can be achieved with this method, albeit with limited control over the path taken. In Diller et al. (2012a), a dynamic stick-slip crawling motion is used to achieve independent but coupled velocity responses. This results in arbitrary positioning of up to three microrobots to goal positions in 2D, following a desired path within a span of a few body-lengths. Vartholomeos et al. (2012) use a similar method which relies on the nonlinear drag of millimeter-scale capsules with different sizes. This method could not be scaled down to the micron-scale due to the reliance on inertial drag forces which are negligible at smaller scales. In Frutiger et al. (2009), multiple resonant magnetic crawling microrobots are designed with different resonant frequencies, allowing for independent motion demonstrated on a specialized electrostatic surface. In a related addressing concept (Diller et al., 2012b), multiple magnetic materials with differing magnetic hysteresis properties are used to achieve independent control of microbotic elements using large magnetic field pulses to selectively turn each element on or off.

While some of these methods show promise for the distributed operation of many microrobots as a team, the limitation to operation on a (2D) surface is significant as further developments in microrobots, especially for medical applications, will require 3D motion in liquid media. Microrobot motion in 3D powered by applied magnetic fields has been accomplished in two ways: swimming by tail rotation or undulation and direct pulling by magnetic field gradients. In swimming, often inspired by bacterial propulsion, a magnetic torque spins an asymmetric structure such as a helix, generating forward thrust in a holonomic manner (Ghosh and Fischer, 2009; Zhang et al., 2009a,b). Such devices all receive the same driving fields and so move in a parallel fashion. While recent results have begun to observe unique rotational step-out behavior for different helical designs, where the microrobot motion decouples with the applied field for high rotation frequencies (Fountain et al., 2010), this method has not been used to achieve independent control of multiple swimming microrobots. Zhang et al. (2009b) have shown the differing velocity response of unique artificial flagella with differing drag torque or magnetic properties, but have not achieved independent

positioning of multiple microrobots, presumably due to the inherent difficulties in controlling such swimming microrobots. Tottori et al. (2011) have used an oscillating magnetic field to independently drive two artificial flagella swimming microrobots with different soft magnetic head designs. This method has also not been used to achieve independent positioning of multiple microrobots.

In the magnetic pulling method for 3D control, a spatial magnetic field gradient is used to directly apply forces to the magnetic microrobot body. This method has shown promise for controlled non-holonomic motion with three translational degrees of freedom, resulting in navigation and micro-object manipulation (Elbuken et al., 2009; Khamesee et al., 2002; Kummer et al., 2010; Meeker et al., 1996). The magnetic pulling method is particularly appealing for medical applications because it could take advantage of existing MRI machines for clinical use (Arcese et al., 2011; Belharet et al., 2011; Kosa et al., 2008; Martel et al., 2007; Mathieu et al., 2006). However, the addressable magnetic pulling of more than one microrobot has not been presented in the literature because all microrobots receive the same driving fields and field gradients. To control multiple microrobots independently in 3D, the typical selective trapping method cannot be used because it relies on a nearby functionalized surface to provide trapping forces. Thus, the use of independent responses of heterogeneous microrobot designs is the only viable method for independent control in arbitrary 3D environments.

In this work, we present the first microrobot addressing method for 3D motion control, which works by magnetic gradient pulling. This method allows for completely independent and uncoupled net forces to be applied to each microrobot and thus allows for sophisticated feedback position control of several microrobots in 3D. The differentiation of magnetic forces applied to each microrobot is accomplished by controlling the unique viscous drag on each unique microrobot when placed in a rotating magnetic field. The different rotational responses result in each microrobot assuming a unique orientation in space. When multiple microrobots with different orientations are placed in the same spatial magnetic gradient field they will experience forces in different directions.

In this paper, we show that any arbitrary 3D force on each unconstrained microrobot can be achieved if the orientation of each microrobot is unique and known. We propose to control and differentiate the orientation by rotating the magnetic field, creating a unique phase lag in each microrobot depending on its magnetic strength and fluid drag characteristics, as shown in Fig. 1(a). Thus, if each microrobot possesses a different magnetic strength or rotational fluid drag coefficient, arbitrary forces can be exerted on each independently and simultaneously when averaged over one short field cycle, as shown in Fig. 1(b). While it is difficult to intuitively study the relationship between such microrobot angles and their resulting force directions in 3D, we will develop such relationships mathematically. Similar dynamic control has been used to manage the magnetic force on a magnetic sphere propelled by a single permanent magnet actuator (Mahoney and Abbott, 2011), but was not used to exert simultaneous unique forces on independent magnets.

Here, we study the physics and implementation of the proposed control method, optimizing the control parameters for best performance. As a demonstration, we show the control of two and three microrobots in a variety of fluid conditions, analyze the effects of nearby walls and calibration errors, and propose several control schemes based on visual feedback to handle the resulting disturbances. The forces on each microrobot are shown to be precise enough for sophisticated simultaneous path following of two microrobots along arbitrary desired paths in 3D. To generalize the results, we also investigate the requirements

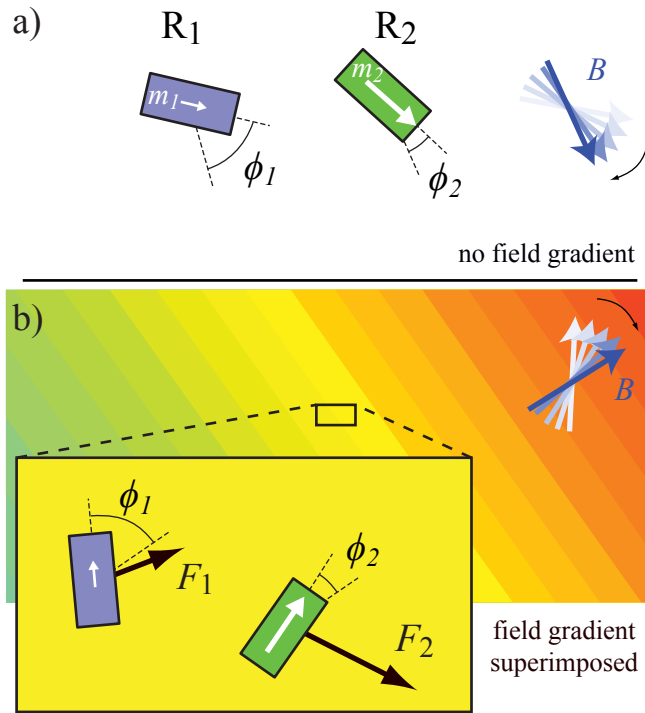


Figure 1: Schematic showing the method to achieve independent orientation control of two microrobots, where the microrobot angle is controlled by the rotation lag in a viscous fluid. (a) Here, R_2 has a strong magnetic moment, and nearly aligns with the rotating field B with phase lag ϕ_2 . Microrobot R_1 has a weak magnetic moment, and thus experiences a large lag angle ϕ_1 . For a constant field rotation rate these angles are constant. (b) Placed in a superimposed magnetic field gradient, the resulting force directions are shown as arrows for a snapshot in time. These forces are unique for a given microrobot moment orientation and magnitude in time. As a 3D field gradient is difficult to visualize, the gradient field shown here is simply a conceptual representation. The inset illustrates that the magnetic field is treated as uniform over the microrobot workspace, although the gradient is non-zero.

for independent control of even larger groups of microrobots using this method. The tradeoffs of the presented control method when compared with single-microrobot control are a reduction in the forces achievable, a small disturbance in the applied force during the field rotation and a loss of microrobot orientation control.

Because it can be executed in nearly any fluid environment using remote magnetic coils, the proposed multi-robot control approach can allow teams of microrobots to share a workspace in micro-fluidic channels or inside the human body for coordinated completion of tasks such as distributed sensing, drug delivery or parallel object manipulation and assembly.

The microrobots used in this study are roughly $400\text{--}4000\ \mu\text{m}$ in size. We have chosen this size scale for ease of fabrication and handling, but believe that the control methods presented here are applicable for smaller magnetic microrobots down to tens of micrometers in size, which experience similar force regimes (in particular, low Reynolds number flow). This method is not expected to work in the nanometer size regime as our assumptions of continuous media and ferromagnetic magnetic responses may begin to lose validity.

The paper is organized as follows: Section 2 introduces the theoretical basis for the simultaneous control of multiple microrobots and outlines the methods for feedback control of multiple microrobots. Section 3 characterizes the experimental setup and microrobot motion. Section 4 gives experimental demonstrations of multi-robot feedback control, and the paper is concluded in section 5.

2 Concept

Magnetic forces and torques are applied to move a microrobot using fields applied from magnetic coils outside the workspace. The magnetic force \vec{F}_m exerted on a microrobot with magnetic moment \vec{m} in a magnetic field \vec{B} , assuming no electric current is flowing in the workspace, is given by

$$\begin{aligned}\vec{F}_m &= (\vec{m} \cdot \nabla) \vec{B} \\ &= \left(\frac{\partial \vec{B}}{\partial x} \quad \frac{\partial \vec{B}}{\partial y} \quad \frac{\partial \vec{B}}{\partial z} \right)^T \vec{m},\end{aligned}\tag{1}$$

and the magnetic torque \vec{T}_m is given by

$$\vec{T}_m = \vec{m} \times \vec{B}.\tag{2}$$

The magnetic field and its spatial gradients depend linearly on the currents through the coils (Kummer et al., 2010), and so the field and gradient terms can be expressed as

$$\vec{B} = \mathbf{B}\vec{I},\tag{3}$$

$$\frac{\partial \vec{B}}{\partial x} = \mathbf{B}_x \vec{I}; \quad \frac{\partial \vec{B}}{\partial y} = \mathbf{B}_y \vec{I}; \quad \frac{\partial \vec{B}}{\partial z} = \mathbf{B}_z \vec{I},\tag{4}$$

where each element of \vec{I} is current through each of the c coils, \mathbf{B} is a $3 \times c$ matrix mapping these coil currents to the magnetic field vector \vec{B} and \mathbf{B}_x , \mathbf{B}_y , \mathbf{B}_z are the $3 \times c$ matrices mapping the coil currents to the magnetic field spatial gradients in the x , y and z directions, respectively. These mapping matrices are calculated for a given coil arrangement by treating the coils as magnetic dipoles in space and are calibrated through workspace measurements as outlined in refs. (Kummer et al., 2010; Meeker et al., 1996).

Thus, for a desired field and force on a single magnetic microrobot we arrive at

$$\begin{bmatrix} \vec{B} \\ \vec{F} \end{bmatrix} = \begin{bmatrix} \mathbf{B} \\ \vec{m}^T \mathbf{B}_x \\ \vec{m}^T \mathbf{B}_y \\ \vec{m}^T \mathbf{B}_z \end{bmatrix} \vec{I} = \mathbf{A}\vec{I},\tag{5}$$

where \mathbf{A} is the $6 \times c$ matrix mapping the coil currents \vec{I} to the field \vec{B} and force \vec{F} . The equation can be solved if the \mathbf{A} is full rank, i.e. the number of coils c is greater than or equal to 6. The solution can be accomplished for $c \neq 6$ through the pseudo-inverse, which finds the solution that minimizes the 2-norm of \vec{I} as

$$\vec{I} = \mathbf{A}^+ \begin{bmatrix} \vec{B} \\ \vec{F} \end{bmatrix}.\tag{6}$$

If $c < 6$, then the solution will be a least-squares approximation. Having greater than 6 coils leads to a better conditioned \mathbf{A}

matrix, which means a more isotropic workspace, reduction of singularity configurations and lower coil current requirements.

Control of the forces and torques on a single microrobot operating in 3D has been previously demonstrated (Kummer et al., 2010; Meeker et al., 1996), with coil currents calculated according to eq. (6). Precise path-following was accomplished in 3D for microrobots from hundreds of microns to several mm in size but no method for the control of more than one microrobot was given in these works.

2.1 Multiple Microrobots

The control problem can be extended to n number of microrobots with magnetization vectors $\vec{m}_1, \vec{m}_2 \dots \vec{m}_n$ and corresponding desired forces $F_1, F_2 \dots F_n$ as

$$\begin{bmatrix} \vec{B} \\ \vec{F}_1 \\ \vdots \\ \vec{F}_n \end{bmatrix} = \begin{bmatrix} \mathbf{B} \\ \vec{m}_1^T \mathbf{B}_x \\ \vec{m}_1^T \mathbf{B}_y \\ \vec{m}_1^T \mathbf{B}_z \\ \vdots \\ \vec{m}_n^T \mathbf{B}_x \\ \vec{m}_n^T \mathbf{B}_y \\ \vec{m}_n^T \mathbf{B}_z \end{bmatrix} \vec{I} = \mathbf{A}^* \vec{I}. \quad (7)$$

with solution

$$\vec{I} = \mathbf{A}^{*+} \begin{bmatrix} \vec{B} \\ \vec{F}_1 \\ \vdots \\ \vec{F}_n \end{bmatrix} \quad (8)$$

where \mathbf{A}^* is a $(3n + 3) \times c$ matrix. The matrix \mathbf{A}^* is full rank if there are $3n + 3$ or more coils. In addition, to achieve a full rank \mathbf{A}^* , all moment vectors \vec{m} must be linearly independent, by possessing different orientations.

To achieve independent orientations of each microrobot (linearly independent \vec{m}), they are placed in a rotating field. If each microrobot is designed to respond differently to this field, they will assume different orientations. As a simple case, a constant magnitude field rotating about an axis defined by rotating the z -axis with the rotation matrix \mathbf{R} is used. The field rotation around this axis is then parameterized by the rotation angle $\theta = |\vec{\omega}|t$ as

$$\vec{B}(\theta) = \mathbf{R} \begin{bmatrix} \cos(\theta) \\ \sin(\theta) \\ 0 \end{bmatrix}, \quad (9)$$

where $\vec{\omega}$ defines the rotation rate and axis and

$$\mathbf{R} = \begin{bmatrix} 1 & 0 & 0 \\ 0 & \cos \alpha & -\sin \alpha \\ 0 & \sin \alpha & \cos \alpha \end{bmatrix} \begin{bmatrix} \cos \beta & 0 & \sin \beta \\ 0 & 1 & 0 \\ -\sin \beta & 0 & \cos \beta \end{bmatrix}, \quad (10)$$

where α and β signify Euler angle rotations about the x and y axes, respectively. To differentiate the unique microrobots, they are designed with different viscous fluid drag and magnetic properties, such that each will assume a different lag angle behind the field direction.

Over one complete rotation the mean magnetic force is therefore given by

$$\begin{bmatrix} \langle \vec{F}_1 \rangle \\ \vdots \\ \langle \vec{F}_n \rangle \end{bmatrix} = \frac{1}{2\pi} \int_0^{2\pi} \begin{bmatrix} \vec{m}_1^T(\theta) \mathbf{B}_x \\ \vec{m}_1^T(\theta) \mathbf{B}_y \\ \vec{m}_1^T(\theta) \mathbf{B}_z \\ \vdots \\ \vec{m}_n^T(\theta) \mathbf{B}_x \\ \vec{m}_n^T(\theta) \mathbf{B}_y \\ \vec{m}_n^T(\theta) \mathbf{B}_z \end{bmatrix} \vec{I}(\theta) d\theta \quad (11)$$

where $\vec{I}(\theta)$ is now varying over the cycle. By equating the average forces over a rotation with the desired forces, we have relaxed the problem slightly as the instantaneous force at any point in time will not equal the desired forces. The averaged force will be an adequate substitute for the desired force if the rotation rate is sufficiently fast compared with the microrobot translation speed. Thus, small deviations in path will occur on the order of the distance traveled during one cycle. As the rotation rate can be controlled, these error can be minimized to below the acceptable error tolerance by increasing the rotation rate.

Equation (11) cannot be solved analytically for $\vec{I}(\theta)$ because the pseudoinverse is not a linear operator, so we discretize the integral into g values of θ for the range $[0, 2\pi)$. This leads to a linear equation which contains the field $[\vec{B}_{\theta_1} \dots \vec{B}_{\theta_g}]^T$ at each rotation step as well as the average force on each microrobot as

$$\begin{bmatrix} \vec{B}_{\theta_1} \\ \vdots \\ \vec{B}_{\theta_g} \\ \langle \vec{F}_1 \rangle \\ \vdots \\ \langle \vec{F}_n \rangle \end{bmatrix} = \frac{1}{g} \mathbf{A}_\theta^* \vec{I}_\theta, \quad (12)$$

where \mathbf{A}_θ^* is the $(3g + 3n) \times cg$ augmented matrix given by

$$\mathbf{A}_\theta^* = \begin{bmatrix} \mathbf{B} & \dots & \mathbf{0} \\ \mathbf{0} & \ddots & \mathbf{0} \\ \mathbf{0} & \dots & \mathbf{B} \\ \vec{m}_1^T(\theta_1)\mathbf{B}_x & \dots & \vec{m}_1^T(\theta_g)\mathbf{B}_x \\ \vec{m}_1^T(\theta_1)\mathbf{B}_y & \dots & \vec{m}_1^T(\theta_g)\mathbf{B}_y \\ \vec{m}_1^T(\theta_1)\mathbf{B}_z & \dots & \vec{m}_1^T(\theta_g)\mathbf{B}_z \\ \vdots & \vdots & \vdots \\ \vec{m}_n^T(\theta_1)\mathbf{B}_x & \dots & \vec{m}_n^T(\theta_g)\mathbf{B}_x \\ \vec{m}_n^T(\theta_1)\mathbf{B}_y & \dots & \vec{m}_n^T(\theta_g)\mathbf{B}_y \\ \vec{m}_n^T(\theta_1)\mathbf{B}_z & \dots & \vec{m}_n^T(\theta_g)\mathbf{B}_z \end{bmatrix}, \quad (13)$$

\vec{I}_θ is the set of current vectors at each value of g of length cg as

$$\vec{I}_\theta = \begin{bmatrix} \vec{I}_{\theta_1} \\ \vec{I}_{\theta_2} \\ \vdots \\ \vec{I}_{\theta_g} \end{bmatrix}, \quad (14)$$

and the moment vector of the i th microrobot is given as

$$\vec{m}_i(\theta_j) = \mathbf{R} \begin{bmatrix} \cos(\theta_j - \phi_i) \\ \sin(\theta_j - \phi_i) \\ 0 \end{bmatrix}. \quad (15)$$

Here, ϕ_i is the constant lag angle of the magnetic moment behind the applied field, as investigated in the next section. The solution to eq. (12) is found using the pseudo-inverse as

$$\vec{I}_\theta = g\mathbf{A}_\theta^{*+} \begin{bmatrix} \vec{B}_{\theta_1} \\ \vdots \\ \vec{B}_{\theta_g} \\ \langle \vec{F}_1 \rangle \\ \vdots \\ \langle \vec{F}_n \rangle \end{bmatrix}. \quad (16)$$

Eq. (16) gives the average magnetic force over the rotation cycle, and can be solved exactly for any number of coils greater

than $(3n+3)/g$ assuming that all magnetic moment vectors \vec{m} are independent. If g is large, the number of coils can be relatively small, and eq. (16) will be an exact solution.

The angles α and β which determine the axis of rotation influence the solution of eq. (16) because the coil system is not isotropic, leading to different solutions requiring different current values. The optimal values of α and β , which minimize the currents $\vec{I}(\theta)$, can be found by optimization.

2.2 Magnet Lag Angles

The lag of a permanent magnet microrobot in a spinning magnetic field is determined by the balance between the applied magnetic torque and the drag torque. Fluid flow at the micro-scale is dominated by viscous forces as opposed to inertial forces, with typical Reynolds numbers of 0.01 or lower for the microrobot size scales around or smaller than 1 mm. The magnetic torque is given by eq. (2), and is proportional to the sine of the angle ϕ between the magnetization and the applied field. The drag torque, assuming Stokes flow and an elliptical microrobot shape with major axis a and minor axis b , is given as (Valberg and Butler, 1987)

$$\vec{T}_d = -\kappa V \mu \vec{\omega}, \quad (17)$$

where κ is the *particle shape factor*, given as

$$\kappa = \frac{1.6 [3(a/b)^2 + 2]}{1 + \zeta - 0.5\zeta(b/a)^2}, \quad (18)$$

where

$$\zeta = \frac{1}{\epsilon^3} \left[\ln \left(\frac{1 + \epsilon}{1 - \epsilon} \right) - 2\epsilon \right] \quad (19)$$

and

$$\epsilon = \sqrt{1 - (b/a)^2} \quad (a \geq b). \quad (20)$$

Here, $V = \frac{\pi ab^2}{6}$ is the volume of the microrobot and μ is the viscosity.

Thus, the balance of torque on the microrobot is satisfied by

$$\vec{T}_m + \vec{T}_d = 0, \quad (21)$$

leading to a relationship for the lag angle ϕ of

$$\sin \phi = \frac{\kappa V \mu |\vec{\omega}|}{|\vec{m}| |\vec{B}|}. \quad (22)$$

For small values of ϕ , this relationship can be simplified to a linear approximation as

$$\phi = C \frac{\mu |\vec{\omega}|}{|\vec{B}|}, \quad (23)$$

where the lag angle constant C linearly relates the lag angle to the ratio $\mu |\vec{\omega}| / |\vec{B}|$. Thus the lag angle constant C must be

determined for each microrobot to achieve control. It should be noted that eq. (22) is not defined for $\frac{\kappa V}{|\vec{m}|} \frac{\mu|\vec{\omega}|}{|\vec{B}|} > 1$, for which the magnetic torque cannot balance the drag torque, and so the microrobot will “step out”, which is characterized by unpredictable oscillations.

If a spherical microrobot is made from soft magnetic material, it could potentially experience no magnetic torque as the magnetization rotated internally. Such a shape and material possesses no magnetic hysteresis and the magnetic moment tends to align with the applied field with no delay. Non-spherical shapes do not possess this characteristic due to demagnetizing fields inside the magnetic material which introduce preferred or “easy” magnetization axes, and thus experience magnetic torques depending on their orientation in a field (Cullity and Graham, 2008). Although it is difficult to fabricate homogeneous microrobots with exact spherical shape, small amounts of isotropy would only result in small torques, and so could potentially be tolerated. Thus, the use of soft magnetic materials is another method of introducing unique magnetization orientations to a set of microrobots in a rotating field.

By varying the parameters $|\vec{m}|$, a , and b between multiple microrobots, the lag angles can be set to different values, and can be varied in real time by changing the value $|\vec{\omega}|/|\vec{B}|$. For use in eq. (16), the ratio of rotation rate to magnetic field strength $|\vec{\omega}|/|\vec{B}|$ can be found which leads to the lowest coil current requirements. This will depend on the desired force vectors. Typically, if all the desired forces are nearly parallel with each other, the lag angles should be similar, meaning a small $|\vec{\omega}|/|\vec{B}|$, but if the desired forces are pointing in opposite directions, then the lag angles should be relatively different, meaning a large $|\vec{\omega}|/|\vec{B}|$, with the maximum value of ϕ staying below the limit of 90° .

2.3 Lag Angle Calibration

The value of the lag angle coefficient C for each microrobot is found through an indirect measurement of the microrobot motion direction. Because observing the microrobot lag angle directly using machine vision is difficult, an indirect method using microrobot position and velocity is preferred. The microrobot is placed in the chosen fluid far from any walls to avoid wall effects. The lag angle can be determined by running the system with arbitrary parameters and observing the microrobot motion direction, which we assume to align with the force direction. Equations (12-15) can then be numerically solved for the lag angle ϕ . However, to avoid solving these equations numerically in real time, a single lag angle with associated force direction is chosen, and the system seeks this force direction. In this way, we can also choose a force vector which will result in high calibration precision. Only one microrobot is calibrated at a time, the coil currents are calculated with $n = 2$ using eq. (16) for the desired perpendicular forces

$$\begin{bmatrix} \langle \vec{F}_1 \rangle \\ \langle \vec{F}_2 \rangle \end{bmatrix} = \begin{bmatrix} 0.05 \\ 0 \\ 0 \\ 0 \\ 0.05 \\ 0 \end{bmatrix} \mu\text{N} \quad (24)$$

using target lag angles of $\phi_1 = 0^\circ$ and $\phi_2 = \phi_c (\neq 0)$. The target lag angle ϕ_2 is typically chosen as 30° . The behavior of the microrobot in this field is used as feedback to calibrate the lag angle coefficient. A microrobot with lag angle of $\phi = 0^\circ$ will move in the x -direction, while a microrobot with lag angle of ϕ_c will move in the y -direction. The microrobot motion direction is observed by differentiating the filtered microrobot detected position. To calibrate the microrobot, the value of $|\vec{\omega}|/|\vec{B}|$ is iteratively varied to change the actual lag angle until the microrobot moves in the y -direction, therefore possessing the lag angle ϕ_c . At this point, the converged value of $|\vec{\omega}|/|\vec{B}|$ is used to calculate the calibrated C as

$$C = \frac{\phi_c}{\mu|\vec{\omega}|/|\vec{B}|}. \quad (25)$$

This calibrated value C is unique to the microrobot design, but is not dependent on the fluid used as the viscosity μ is pulled out of C .

2.4 Wall Effects

When operating in fluid near a solid boundary, the torque required to rotate a microrobot increases. Liu and Prosperetti (2010) studies a sphere of diameter D rotating about an axis perpendicular to a planar boundary in low Reynolds number environment, giving a far-field approximation for the increase in torque from the unbounded fluid torque T_d to the torque in the presence of the wall T_w at a distance d from the wall as the ratio

$$T_w/T_d = [1 - \frac{1}{64} \left(\frac{D}{d}\right)^3 - \frac{3}{65536} \left(\frac{D}{d}\right)^8]^{-1}, \quad (26)$$

with a value of 1.202 being the exact maximum torque ratio when in contact with the wall. For a sphere rotating about an axis parallel to the boundary, the far-field approximation gives

$$T_w/T_d \approx 1 + \frac{5}{128} \left(\frac{D}{d}\right)^3. \quad (27)$$

These far-field equations are accurate for values of $\frac{D}{d}$ greater than approximately 1.2.

For a nonspherical shape like those of the microrobots in this study, an equivalent diameter is used to calculate the wall effects. The microrobot short axis a is used in the case of rotation about a perpendicular axis and b is used for rotation about a parallel axis.

When near a wall, a microrobot rotation axis which is not perpendicular to the wall can also result in a fluid force parallel to the wall (Liu and Prosperetti, 2010). To mitigate this additional fluid force, the microrobot rotation axis can be held perpendicular (or nearly perpendicular) to the wall. This may reduce the optimality of the solution found using eq. (12), but avoids the complication of difficult-to-predict fluid drag forces.

2.5 Alternative Field Motions

In section 2.2 we introduced a constant magnitude rotating field as a simple case which results in a constant lag angle during rotation. This waveform results in satisfactory performance for controlling one or two microrobots, with a well-conditioned matrix \mathbf{A}^* and relatively simple lag angle calculation using eq. (23). However, due to the steady-state nature of this waveform, the actuation matrix drops rank (by $3n$) when controlling more than two microrobots. This is because all of the magnetization vectors are linearly dependent in a 2D plane (even though they are constantly rotating, the magnetization vectors are all multiplied by the same rotation matrix \mathbf{R} in eq. (15)). Therefore, the solution to eq. (16) for $n > 2$ results in an inexact approximation to the desired force vectors.

To keep \mathbf{A}^* from dropping rank, we need increased independence of the magnetization vectors. We can achieve this by using a waveform which gives a time-varying relation between the lag angles. Thus, a solution with a transient or intermittent component can be used, with one candidate being a rocking field of constant magnitude.

To solve for the microrobot orientation as a function of the applied field for any arbitrary applied field $\vec{B}(t)$, we solve the first-order differential equation for the microrobot rotation axis $\vec{\omega}(t)$

$$\kappa V \mu \vec{\omega}(t) = \vec{m} \times \vec{B}(t), \quad (28)$$

which simplifies if the applied field is constrained to a plane to

$$\kappa V \mu \frac{d\phi(t)}{dt} = |\vec{m}| |\vec{B}|(t) \sin [\theta(t) - \phi(t)], \quad (29)$$

where ϕ is the microrobot orientation in the plane and θ is the field orientation in the plane.

This equation was solved exactly in section 2.2 for a constant field rotation, but for arbitrary field inputs (such as the rocking field cycle), it must be solved numerically. The result of such a numerical solution using Matlab's ode45 function is shown in Fig. 2 for three microrobots with evenly distributed length ratios a/b of 1.0, 2.0 and 3.0, resulting in the microrobot lag angles $\phi_1(t)$, $\phi_2(t)$ and $\phi_3(t)$, respectively. It can be seen here that the lag angles are independent and varying with respect to each other over time in a nonlinear fashion, which results in a full-rank \mathbf{A}^* matrix.

The downside of using this rocking field cycle compared with the constant rotation case is a reduction in the angle discrepancy between the microrobots. This results in a more poorly conditioned \mathbf{A}^* matrix and therefore, lower attainable microrobot forces. In addition, the solution of eq. (28) requires additional computation which must be performed online for tasks such as feedback control of microrobots which require constantly changing desired forces.

Other field waveforms could be applied, such as a step, impulse, or randomly ‘‘wandering’’ fields, but are not investigated in this work.

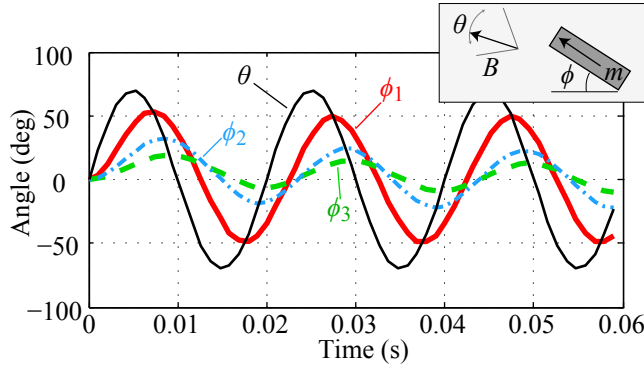


Figure 2: Response of three microrobots to a planar constant magnitude rocking field input with strength 2.0 mT and peak to peak rocking amplitude of 70°. Here, the frequency of rocking is 50 Hz.

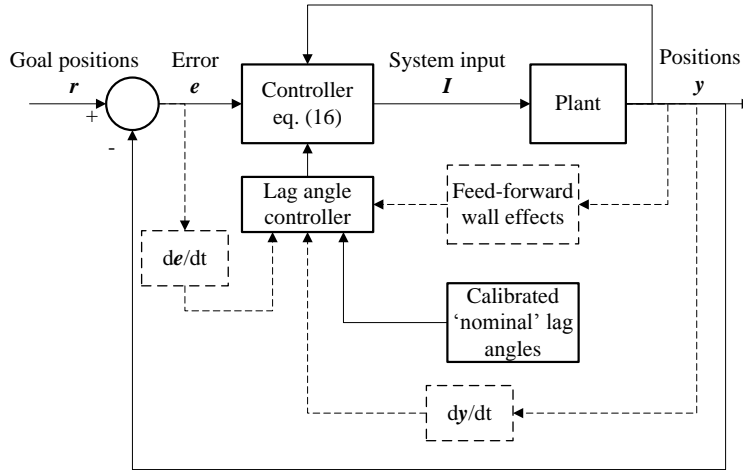


Figure 3: Multi-microrobot feedback controller. The dashed feedback elements are the optional lag angle feedback and feed-forward wall effects.

2.6 Feedback Control Design

To effectively control multiple microrobots in 3D, a vision-based feedback controller is implemented. Using cameras viewing from the ‘top’ and ‘side’ orientations, the 3D positions of the microrobots are tracked. The goal positions $\vec{r} = \begin{bmatrix} \vec{r}_1^T & \dots & \vec{r}_n^T \end{bmatrix}^T$ of all n microrobots are specified as user or high-level controller input. The actual positions \vec{y} are used to calculate the position error $\vec{e} = \vec{r} - \vec{y}$, which is fed to the system controller. This calculates coil currents \vec{I}_θ using eq. (16), where the desired force vectors are held proportional to the error vector by a constant gain K as $\vec{F} = K\vec{e}$. This proportional feedback loop is outlined schematically in Fig. 3. As eq. (16) is relatively computationally intensive, the calculation is not instantaneous. In addition, each time the coil currents are recalculated the rotation axis must be changed, resulting in a disrupting reorientation. These two factors mean that the feedback control rate must be slowed to several times slower than the rotation rate. This very slow feedback rate precludes the use of an integral feedback term for navigation in small workspaces where the system may only recalculate the coil currents a few times before the commanded direction is changed. However, in different conditions an integral term could improve control performance.

Lag angles are pre-calibrated using the method discussed in section 2.3. As an optional feedback component, the lag angles

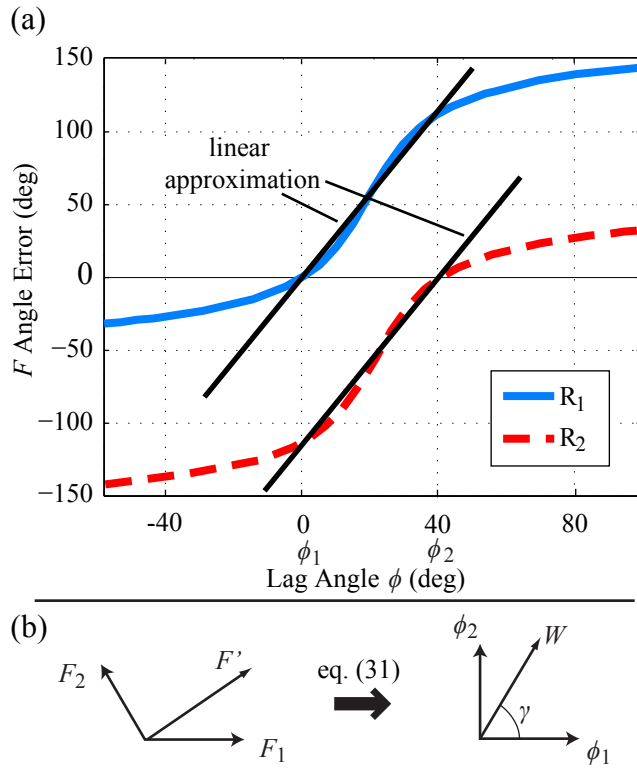


Figure 4: Error in lag angle: (a) Effect of lag angle error on error in the resulting force for two microrobots. Here the calibrated lag angles are $\phi_1 = 0^\circ$ and $\phi_2 = 40^\circ$ and the desired forces are $\vec{F}_1 = [0 \ 0.05 \ 0]^T \mu\text{N}$ and $\vec{F}_2 = [0.05 \ 0 \ 0]^T \mu\text{N}$ for R_1 and R_2 , respectively. F angle error is taken as the angle between the resulting force and the desired force. (b) The observed force \vec{F}' is transformed into the (ϕ_1, ϕ_2) space, where the actual lag angle ϕ' can be calculated. The out-of-page \vec{N} component is not shown for clarity.

can be updated by observing the error in the microrobot motion directions $\angle \vec{y}$ from the desired force directions $\angle \vec{F}$. An error in this angle implies that the lag angle calibration is incorrect, and can be fed back to the lag angle controller. If the actual force direction is assumed to be parallel to the microrobot motion direction, the force on each microrobot can be observed by the derivative of the positions as $\vec{F} \propto d\vec{y}/dt$. If it is assumed that the error in the force direction is proportional to the error in the lag angle, the lag angle can be found in one computation. This assumption is valid for some cases (it is most accurate when all desired forces are nearly parallel), but for other cases it is less accurate. Fig. 4(a) shows the actual force directions as a function of lag angle in a ‘worst’ case, for nearly-perpendicular desired forces on two microrobots. In this case, the linearity assumption is most accurate for positive lag angle errors for microrobot R_1 and negative lag angle errors for R_2 , i.e. for lag angles between the two desired lag angles.

Using the linearity assumption for two microrobots, a linear relation can be created which maps the observed motion directions $d\vec{y}/dt$ to the actual lag angles. When the applied field is constrained to a plane as it rotates, the force directions are also constrained to a different plane defined by the vectors \vec{F}_1 and \vec{F}_2 as the normal vector $\vec{N} = (\vec{F}_1 \times \vec{F}_2) / |\vec{F}_1 \times \vec{F}_2|$. The actual observed microrobot force \vec{F}' can be mapped to the (ϕ_1, ϕ_2) space as the vector \vec{W} by

$$\begin{bmatrix} \vec{F}_1 & \vec{F}_2 & \vec{N} \end{bmatrix} \vec{W} = \vec{F}'. \quad (30)$$

This is shown schematically in Fig. 4(b). The three components of the vector \vec{W} thus contain the \vec{F}_1 , \vec{F}_2 and \vec{N} components of \vec{F}' , and can be found as

$$\vec{W} = \begin{bmatrix} \vec{F}_1 & \vec{F}_2 & \vec{N} \end{bmatrix}^{-1} \vec{F}'. \quad (31)$$

The actual lag angle ϕ' is then found using the first two components of \vec{W} , which define an angle γ in terms of ϕ_1 and ϕ_2 , as

$$\phi' = \phi_1 + \frac{2\gamma}{\phi_2 - \phi_1} = \phi_1 + \frac{2 \tan^{-1}(W_2/W_1)}{\pi(\phi_2 - \phi_1)}, \quad (32)$$

which is then used to bias the calibrated nominal lag angle in the controller. This feedback is used to update the lag angle in the presence of disturbances such as local fluid viscosity changes or wall effects. If more than two microrobots are used, eq. (31) can be generalized to higher dimensions (without the use of the normal vector \vec{N}), and solved using the pseudo-inverse to find an approximate solution for the lag angle ϕ' . Alternately, a more precise lag angle feedback controller which does not rely on the force linearity assumption could be found which numerically calculates the lag angle from the actual observed motion direction using eq. (12). The downside of such an accurate solution is greatly increased computation time, which must be performed online for feedback control.

As a final feedback control element to better deal with wall effects when the wall position is known a-priori, a feed-forward term can be included which uses eqs. (26,27) to update the lag angles proportional to the increase in expected torque. However, the modest increase in drag near the wall precludes the use of such a wall-effect controller except when operating within 1-2 microrobot body-lengths of the wall.

3 System Design and Characterization

3.1 Magnetic Coil Setup

The magnetic microrobots are actuated by eight independent air or iron-core electromagnetic coils shown in Fig. 5, which are aligned pointing to a common workspace center point with an approximate opening size of 12 cm. The currents in the electromagnetic coils are controlled using a PC with data acquisition system at a control bandwidth of 20 kHz, using linear electronic amplifiers (SyRen 25, Dimension Engineering Inc.) and Hall-effect current sensors (ACS714, Allegro Microsystems Inc.). Imaging of the microrobots and workspace is accomplished by two CCD cameras (Foculus F0134SB) connected to variable magnification microscope lenses, providing up to a 26 mm×20 mm field of view from the top and side perspectives. Magnetic flux densities and gradients of up to 8.3 mT and 0.34 T/m, respectively, can be generated in the workspace, with a 3.3× increase when iron cores are inserted into the coils. For a 20 mm×20 mm workspace in the center of the coil system, the field and field gradient is shown to be uniform within 6.0% of the nominal value as measured with a Hall effect sensor (Lakeshore Gaussmeter 410).

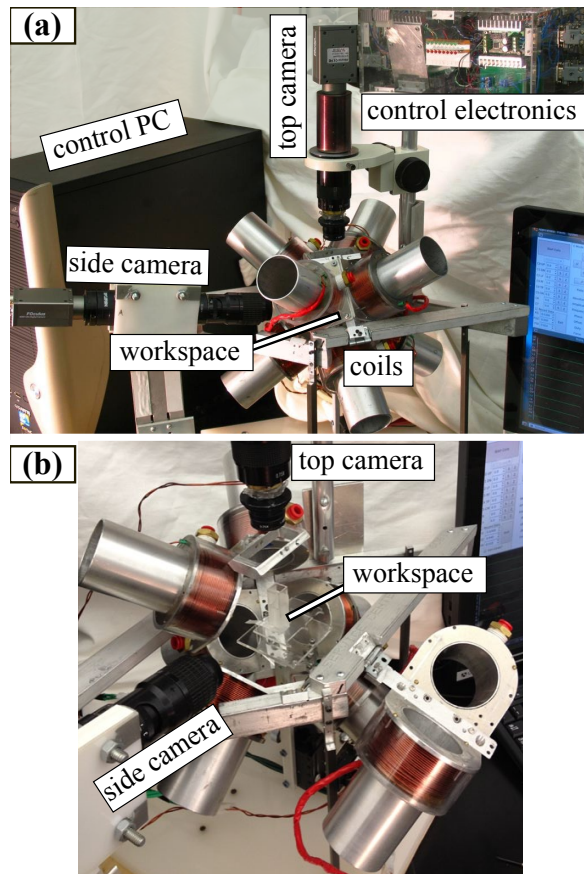


Figure 5: Photograph of the electromagnetic coil setup. (a) All system components are shown with the coils in the operational position. (b) Two coils hinge open to allow for access to the workspace.

Table 1: Electromagnet Properties.

Property	Value	Units
Number of turns	140	—
Resistance	0.4	Ω
Wire diameter	1.15	mm
Coil length	3.2	cm
Inner diameter	5.1	cm
Distance to workspace	4.1	cm
Max driving current	19	A
Max field at workspace (air core)	8.3	mT
Max field gradient at workspace (air core)	0.34	T/m
Iron core amplification factor	$3.3\times$	—

3.2 Microrobots

3.2.1 Fabrication

In this work, individual microrobots are fabricated to be magnetically hard, retaining their internal magnetization in the absence of an externally applied magnetic field, or magnetically soft, with magnetization dependent on the applied field. Microrobots are fabricated in a batch process using soft photolithography and molding techniques in a manner similar to Imbaby et al. (2008). Microrobots are composed of neodymium-iron-boron (NdFeB) particles in a polyurethane matrix, with fabrication details given in Diller et al. (2011a). Due to the high magnetic coercivity of NdFeB (i.e. fields over 600 mT are required to demagnetize NdFeB), these microrobots are not subject to demagnetization from the relatively weak fields applied in this work. Microrobot R₁₁ is fabricated using soft iron as the magnetic material, and it is molded from a rubber mold which is made from glass microspheres glued to a glass slide. The molding process for all microrobots is prone to variations in microrobot geometry (up to $\sim 10\%$ from nominal), but the control method is not sensitive to small geometric changes.

To create unique microrobot designs, microrobots are designed with several sizes, shapes and magnetic properties, as outlined in Table 2 and shown in Fig. 6. Rotational drag is added by the inclusion of non-magnetic polyurethane additions, which are molded or glued directly to the microrobots. The designs designated “cube” are simple magnetic cubes, magnetized to different magnetic moment values. The designs designated “wings” have thin ($\sim 30\ \mu\text{m}$) polyurethane sheets affixed on using UV-curable adhesive to increase rotational fluid drag. Designs designated “cylinder” consist of a “cube” design which is then molded into a larger polyurethane cylinder in a tubular mold.

3.2.2 Design for neutral buoyancy

To aid the experiments, it is advantageous to use neutrally buoyant microrobots, such that the effective weight in liquid is zero. In this case, the only forces acting on the microrobot are magnetic and fluid drag forces, simplifying the force observation and allowing us to easily constrain the microrobots to a small workspace in 3D for easy observation without compensating for weight.

To achieve neutral buoyancy, the average density of the microrobot must be equal to that of the fluid environment. As

Table 2: Microrobot Properties.

	Shape	Dimensions length×width (μm^2)	Magnetic Material	$ \vec{m} $ (μAm^2)	C theoretical (mm/A)	C (mm/A)
R ₁	cube	407 × 394	NdFeB	0.200	1.00	1.58 ± 0.13
R ₂	cube	391 × 391	NdFeB	0.376	0.50	0.61 ± 0.02
R ₃	cube	365 × 350	NdFeB	0.568	0.44	0.44 ± 0.02
R ₄	cube-wings	1010 × 463	NdFeB	0.456	2.76	2.02 ± 0.18
R ₅	cube-wings	1507 × 364	NdFeB	0.342	7.68	6.90 ± 0.46
R ₆	cylinder	2099 × 539	NdFeB	0.471	15.65	12.63 ± 0.91
R ₇	cylinder	1311 × 539	NdFeB	0.569	4.41	4.21 ± 0.03
R ₈	cylinder	3546 × 539	NdFeB	0.480	55.9	48.95 ± 2.57
R ₉	large	687 × 762	NdFeB	1.908	0.62	0.49 ± 0.04
R ₁₀	large-wings	4031 × 650	NdFeB	1.955	20.75	16.72 ± 0.85
R ₁₁	sphere	∅ 430	Fe	–	0.0	~ 0.0

the materials used to create microrobots are of higher density than the fluids used, the density of the microrobots must be reduced. An air pocket is included inside the microrobot through the molding process as shown in Fig. 6(a). The air pocket is “capped” by gluing a thin section of polyurethane over the gaps. The volume of trapped air is approximately 60% of the total microrobot volume, and the overall density is fine-tuned by adding small pieces of dense nonmagnetic material such as polyurethane. Magnetic moment values for neutrally buoyant microrobots are relatively low compared to designs without the included air pocket due to the reduction in magnetic material.

3.3 Lag Angle Verification

When being used in experiments, the microrobot lag angle constants C can be calibrated using the iterative process from section 2.3 which relies only on observing the position and velocity of the microrobot. However, accurate direct measurement of the lag angle is needed to verify this method for each microrobot design. To do this, images of a rotating microrobot are captured using a high speed camera (pco.dimax) through the side-view optics at 300 frames per second. The rotational frequency and field amplitude are selected for the desired $|\vec{\omega}|/|\vec{B}|$ range appropriate for the microrobot, such that the lag angle will vary from 0° to 90° . The high speed images are optically synchronized with the direction of the magnetic field using a blinking LED in the frame of view. The lag angle is measured manually from individual frames in post-processing. As a typical example, Fig. 7 shows the experimentally observed lag angles along with equations (22, 23), for microrobot R₇. The lag angles closely follow the theoretical expected values for all but the largest lag angles. The shaded region indicates the “step-out” regime, for which the lag angle is expected to be widely varying as the microrobot oscillates unpredictably. This region is defined as the values of $\mu|\vec{\omega}|/|\vec{B}|$ for which the lag angle exceeds 90° and eq. (22) cannot be solved. The final two data sets lie in this step-out region, with the last data set showing the expected large variation in lag angles. Operation in this region is avoided.

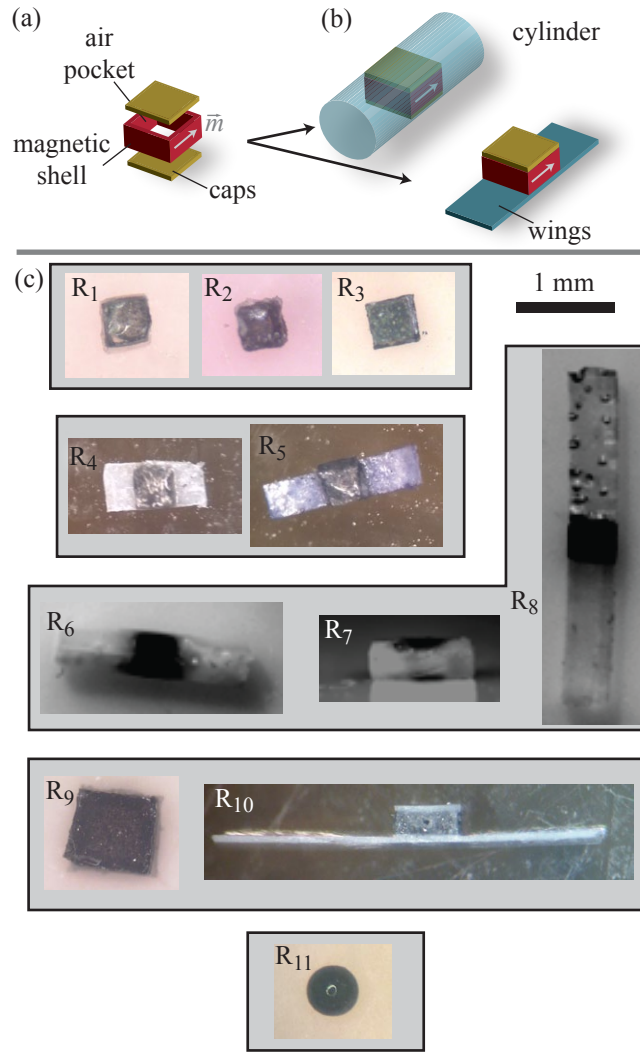


Figure 6: Microrobot designs: (a) The fabrication process for neutrally buoyant heterogeneous designs. A pocket of air is trapped inside a planar magnetic shell by two polyurethane caps which are fixed by adhesive. (b) Optical microscope images of each unique design.

3.3.1 Unique microrobot designs

Table 2 gives the theoretical lag angle constants C for the various microrobot designs as determined by eq. (22). The experimental C values are determined using a least-squares fitting method to 10 data points, with the stated error ranges as a confidence interval of 95%. Sources of error in the experimental lag angle measurements could be inaccurate magnetic field vectors arising from coil current error, non-uniformity over the coil workspace, and direct error in the measurement of the lag angle. In some cases the theoretical C value lies outside of the confidence interval of the experimental data, which could be due to inaccurate microrobot dimensions as well as the assumption of ellipsoidal microrobot shape in eq. (22). These discrepancies highlight the need for experimental calibration of C for each microrobot design.

Microrobot R_{11} , made with soft iron as its magnetic material, has a predicted magnetic lag angle of 0.0, as the magnetization is expected to rotate internally within the microrobot to stay aligned with the applied field without the influence of viscous drag. As this rotation cannot be observed visually, the actual lag angle is experimentally estimated using the automated iterative

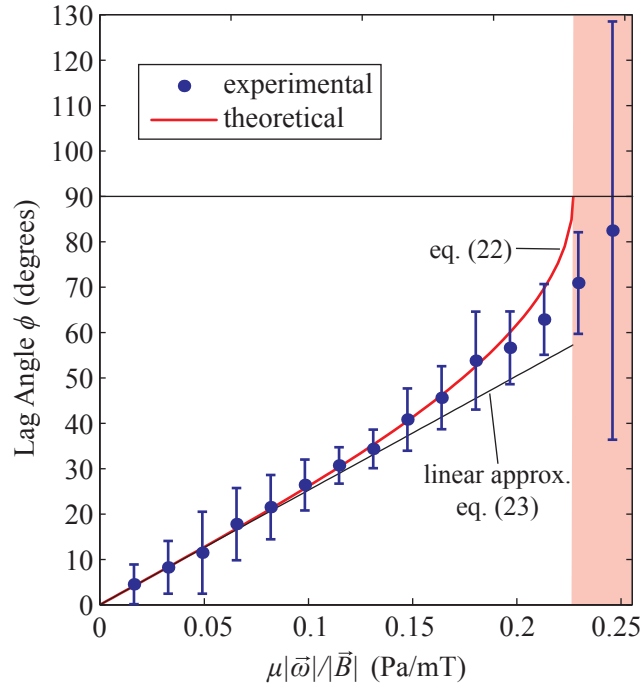


Figure 7: Lag angle as a function of $|\bar{\omega}|/|\bar{B}|$ for microrobot R₇. The theoretical curve is the predicted relationship from eq. (22) using microrobot geometry and magnetic properties from Table 2. The theoretical linear approximation, eq. (23), is seen to be a fair approximation for lag angles up to $\phi = 40^\circ$. The shaded area highlights the region of $\mu|\bar{\omega}|/|\bar{B}|$ for which the microrobot will experience step-out (ϕ exceeds 90°). Each point is an average of 25 data points, 5 points each from 1-5 mT field strength and error bars represent the standard deviation of each set.

process from section 2.3. In this experiment, the applied field magnitude is increased to 3.8 mT to magnetize the iron sample and a relatively high rotation rate of 14.8 Hz was used to force the microrobot to ‘step-out’ mechanically. For a hard-magnet microrobot, such a high rotation rate would lead to no net force exerted as the microrobot orientation unpredictably rocks back and forth. However, for the soft iron sphere, the magnetization is free to rotate internally, closely aligned with the applied field and a clear force is exerted in the desired direction. It should be noted that the microrobot does experience small magnetic torques, and rocks slightly in place during this experiment. Thus, the magnetic lag angle is not exactly zero, but is instead some small value. Future work will further investigate the actual lag angle inside such soft spherical microrobots.

It can be seen from Table 2 that variations in microrobot size, shape and magnetization can lead to significant differences in C , covering two orders of magnitude for the designs presented. This suggests that the presented design variables introduce enough diversity to allow for independent control.

3.4 Optimization and Simulation Results

3.4.1 Operation parameter optimization

The effects of α , β , $|\vec{m}|$, a , b and $|\bar{\omega}|/|\bar{B}|$ values are investigated in simulation, where eq. (16) is solved for the desired forces and the required coil currents \vec{I}_θ are output. As will be seen later, an optimization of these parameters is required to achieve controllable 3D motion of multiple microrobots given limitations in coil strength. To minimize the current required to drive the magnetic coils, we want to minimize the 2-norm of the vector \vec{I}_θ , leading to a nonlinear constrained optimization problem stated

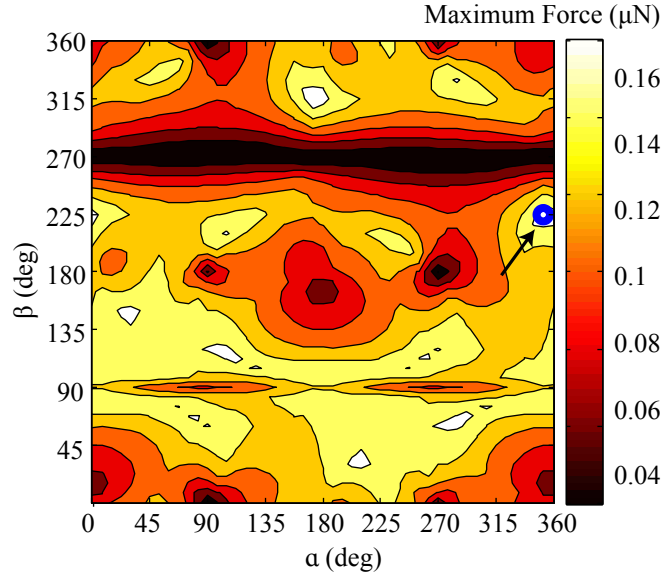


Figure 8: Maximum forces attainable for the rotation axis defined by the Euler angles α and β . The optimal value (highest max force) for the specific set of desired forces found by the gradient descent method is shown with a blue circle.

as

$$\begin{aligned} & \underset{\alpha_e, \beta_e, |\vec{\omega}|/|\vec{B}|}{\text{minimize}} && \|\vec{I}_\theta\|_2^2 \\ & \text{subject to} && I_\theta(j) \leq 19 \text{ A}, \quad j = 1, \dots, cg \end{aligned} \quad (33)$$

where 19 A is the maximum attainable coil current. This can be expressed as an unconstrained nonlinear optimization problem through use of the *barrier method* (Boyd and Lemarechal, 2004) as

$$\underset{\alpha_e, \beta_e, |\vec{\omega}|}{\text{minimize}} \quad \|\vec{I}_\theta\|_2^2 + \sum_{j=1}^{cg} \log [19 \text{ A} - I_\theta(j)], \quad (34)$$

This optimization is implemented through the Newton gradient method (Boyd and Lemarechal, 2004). As the problem is nonconvex, with the possibility for local minimums, we implement the optimization with multiple starting points to increase the chance of finding the global minimum. Results from a search optimization are presented in Figs. 8-10.

Fig. 8 shows the cost function (maximum forces attainable) for the rotation axis defined by the Euler angles α and β . This figure shows that the maximum force achievable varies from $0.04 \mu\text{N}$ to $0.17 \mu\text{N}$ for different rotation axis choices. Thus, performing some kind of optimization to find the best rotation axis has potential to improve performance significantly. The optimal value (highest max force) for the specific set of desired forces found by the gradient descent method is shown with a blue circle and an arrow. The nature of this optimum force map will vary with the desired forces and also with the coil configuration. Indeed, changes to the number of coils could significantly alter this landscape, with more coils tending to smooth the map as the system becomes more isotropic.

In Fig. 9, the calculated forces on two microrobots are shown over two field cycles, for the case of constant field rotation. The desired forces in this case are $\vec{F}_1 = [0 \ 0.02 \ 0.05]^T \mu\text{N}$ and $\vec{F}_2 = [-0.02 \ 0.05 \ 0]^T \mu\text{N}$. The fluid drag on each microrobot is taken as the same but the magnetizations are $|\vec{m}_1| = 3.0 \text{ memu}$ and $|\vec{m}_2| = 2.0 \text{ memu}$ such that the difference in lag angles

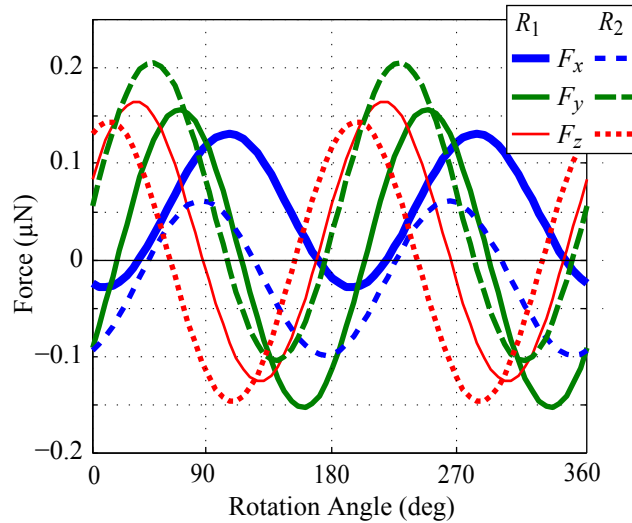


Figure 9: Microrobot force components over two continuous field rotation cycles with two microrobots. Here, the desired (average) forces are $F_1 = [0 \ 0.02 \ 0.05]^T \mu\text{N}$ and $F_2 = [-0.02 \ 0.05 \ 0]^T \mu\text{N}$.

is about 10° . The average of each force curve corresponds to the desired force. It can be seen that the maximum forces exerted exceed the desired (average) forces by a factor of roughly 3. Indeed, the instantaneous force at times even pulls in the opposite direction from the desired force. However, as long as the rotation is executed quickly with respect to the translational speed of the microrobot, these fluctuations will be minor and only the desired force will be observed.

In Fig. 10, the eight coil currents corresponding to the forces shown in Fig. 9 are calculated over one rotation, for the constant field rotation case in (a) and for the rocking field case in (b). In the figure, it can be seen that the coil currents for this optimized case are relatively low (compared with their maximum values of 19 A) and are smooth and continuous over time. The continuous nature of the currents results naturally from the use of the pseudo-inverse in the solution of eq. (16). Indeed, discontinuities would present challenges for implementation in the coil system with finite coil inductance, which does not permit sudden changes in current. The current cycles in Fig. 10(a) for the constant rotation case resemble sinusoids while those in Fig. 10(b) for the field rocking case are more complex in nature. These current values will be recreated in the coils to achieve the forces desired.

3.5 Attainable Microrobot Forces

The microrobots from Table 2 are designed to create a wide range of lag angles in an applied field through varying geometry and magnetic strength. The effect of the degree of heterogeneity of a set of microrobots on their controllability is investigated in Fig. 11 for 1 to 4 microrobots being controlled independently. Here, the maximum force attainable for each of the independent microrobots was determined as a function of the ratio of the lag angles C of a set of microrobots possessing the same magnetic moment but different lengths. Thus, the C ratio serves as a measure of the diversity of the set. We expect microrobot sets with more diversity (smaller C ratios) would be capable of exerting larger forces. Other methods of introducing diversity such as varying the magnetic moments, as with microrobots R_1 - R_3 or using a different magnetic material, such as with R_{11} , would have a similar effect as varying the length.

Here, the max force is calculated in simulation by finding the maximum force attainable in ten different randomly chosen

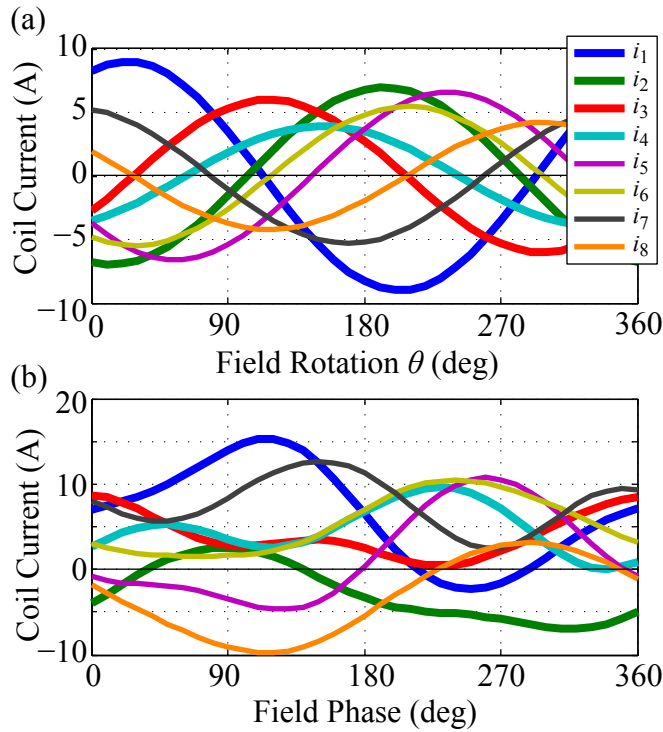


Figure 10: Coil currents for the eight coils for an optimized case. Here, the eight coil currents are calculated over one field cycle for (a) continuous field rotation and (b) rocking field.

directions, and taking the average of each of these maximum values. This averaging is done to reduce the effect of the anisotropy of the system, but masks the fact that some force directions may have much lower maximum force values. For each force direction, the optimal rotation axis is found, and the desired forces on the set of microrobots is increased until the coils exceed their maximum current limit of 19 A. The results are plotted for a range of microrobot length ratios from 0.05 (very different C values) to 0.95 (very similar C values), where the microrobot widths and heights are fixed at $300 \mu\text{m}$ and the magnetic moments are all 0.6 memu. The $n = 1$ and $n = 2$ cases are plotted for the continuous field rotation case. However, as the continuous field rotation cannot be used to control more than two microrobots, the $n = 2, 3$ and 4 cases are plotted for the rocking field presented in section 2.5. As expected, the mean forces attainable for larger sets of microrobots reduces drastically as the actuation matrix becomes more poorly conditioned. For the $n = 3$ and $n = 4$ cases, the microrobot C values are evenly distributed with the ratio of the smallest to the largest microrobot C values being the stated ratio. In these cases, the minimum C ratio between any two microrobots is less than that stated, which contributes to the degradation in performance compared with the cases with fewer microrobots. The estimated threshold minimum force required to maintain robust feedback control (overcoming hardware errors, nonuniformity of the fields over the workspace and buoyant forces) is estimated to be approximately $0.09 \mu\text{N}$, meaning that robustly controlling more than two microrobots in 3D is not possible with the present hardware. A coil system with larger maximum field gradients could increase the achievable forces to control more microrobots. It should be noted for comparison that a single microrobot pulled directly by magnetic gradients (simply calculated using eq. (6)) can achieve a maximum force of about $0.4 \mu\text{N}$ in this simulation.

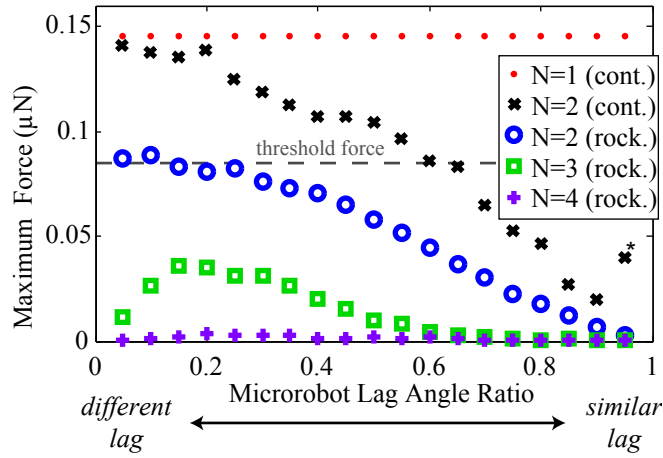


Figure 11: Effect of microrobot diversity on the mean force attainable from simulation when controlling one, two, three or four microrobots. Two styles of applied field are shown, marked ‘cont.’ for the continuous field rotation case, and ‘int.’ for the rocking field case. Small variations in the force are due to the optimization routine, which frequently encounters local minima. The data point indicated with a “*” for $n = 2$ (cont) represents a poorly conditioned \mathbf{A}^* matrix with erroneous solution because the microrobot lengths are so similar. The estimated minimum threshold force of $0.09 \mu\text{N}$ to maintain robust control for the coil hardware is shown as a dotted line.

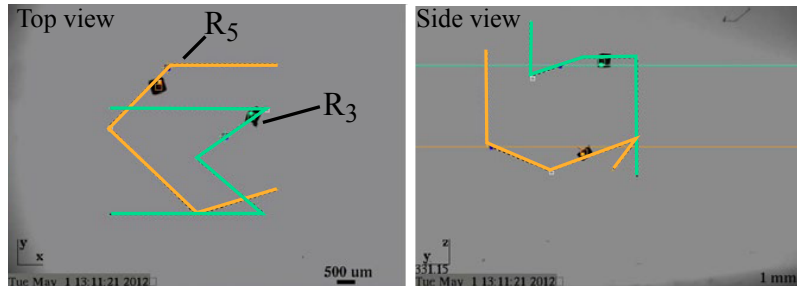


Figure 12: Frame from a video of two microrobots following a desired path in 3D. Computer overlays of the desired path and detected microrobot position are shown in orange and green. Actual microrobot paths are shown in Fig. 13. Video available in Extension 1.

4 Feedback Control Experiments

The feedback control methods are tested experimentally to prove their performance. Control using visual feedback is used to follow desired paths in 3D, and the ability of the feedback to reject disturbances from wall effects and miscalibration are investigated.

4.1 Path Following

Two microrobots (R_3 and R_5) are moved along independent trajectories in 3D space, with a snapshot of the top and side microscope views shown in Fig. 12. Here, the microrobots are controlled using the constant field rotation waveform, with a field rotation rate of 1.2 Hz, at a constant field strength of 1.1 mT, and in oil with viscosity of 50 cSt. The field rotation axis is constantly updated to the optimal choice using the method presented in section 3.4.

The tracked microrobot paths are shown in Fig. 13, where the solid lines show the paths of each microrobot in 3D, from the (a) top view and (b) front view. Circles show the tracked microrobot position every 1.0 s. Here the average path error is found

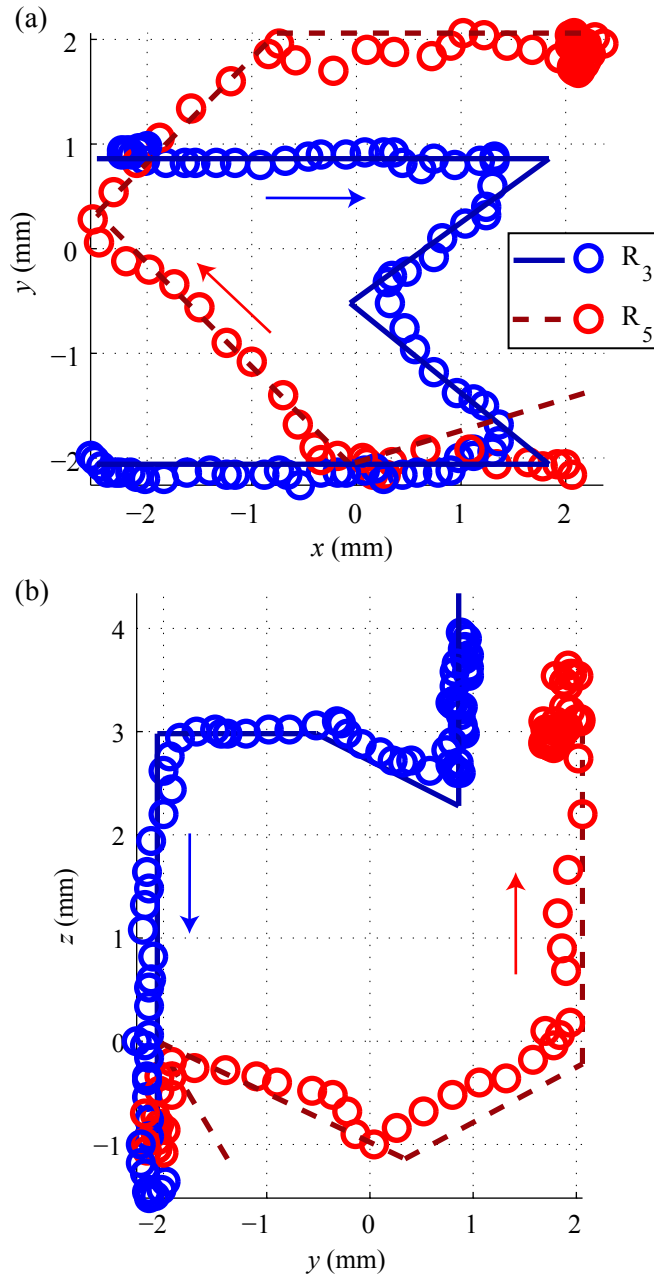


Figure 13: Feedback control for two microrobots following the desired path in silicone oil with a viscosity of 50 cSt for (a) top and (b) front views. Circles show the tracked microrobot position every 1.0 s. Average error from path is 0.23 mm for R_3 and 0.31 mm for R_5 . Video available in Extension 1.

to be 0.23 mm for R_3 and 0.31 mm for R_5 . This relatively low error, which is less than the microrobot body sizes, shows the capability for truly independent control of each microrobot in 3D along precise paths.

The average path error for four microrobot pairs is compared in Table 3 completing the same path from Fig. 13. Stated is the mean and standard deviation for 5 runs of each pair, along with the ratio of lag angles. To ensure a fair comparison, the same controller gains are used for each pair. This results in slightly sub-optimal performance, as compared with the best hand-tuned gains shown used in Fig. 13. From the data, it can be seen that microrobot pairs with very different lag angles (low ratio) follow the path with the least error. This is expected when observing the average loss in applied force given in Fig. 11 for different

Table 3: Average path error for different microrobot pairs.

Microrobots	Lag Angle Ratio	Average Path Error (mm)
R ₁ , R ₅	0.034	0.49±0.10
R ₂ , R ₅	0.048	0.31±0.08
R ₃ , R ₅	0.13	0.38±0.05
R ₅ , R ₁₀	0.41	2.09±0.65*

lag angle ratios. From this figure, it is seen that a lag angle ratio of 0.41 should result in an average force reduction of about 30%, although some desired force directions might be much worse than this average value. In this case, errors from microrobot neutral buoyancy, coil current and feedback control result in very poor path following performance. Indeed, the pair R₅, R₁₀ is marked with an “*” to denote that the pair is only able to complete approximately one half of the path before the coils overheat, forcing the end of the experiment (roughly 5 minutes at full coil power). Microrobot pairs with even larger lag angle ratios are not capable of feedback control due to an even greater reduction in force due to the limitations in the current coil system. Such pairs fall below the “threshold force” line in Fig. 11. In terms of absolute microrobot size, one relatively long microrobot over 1.5 mm was required in these experiments to achieve independent control.

The control of microrobots in lower viscosity liquid is also possible. To achieve similar lag angles, the value of $|\vec{\omega}|/|\vec{B}|$ is increased roughly proportional to the fluid viscosity. In lower viscosity liquid, the motion dynamics are sped up, and thus control with the system hardware becomes limited by the camera feedback rate (40 frames per second). The error when following a rectangular path 3.4 mm on a side in oil of viscosity 5 cSt is 0.48 ± 0.19 mm, with reduced controller gains. The system tends to be unstable for larger gains due to the limited feedback rate. However, these problems could be mitigated by a faster camera frame rate in future experiments. In addition, control in liquids of higher viscosity is also possible, with a reduction in $|\vec{\omega}|/|\vec{B}|$ and motion speed. Experimentally we have performed multi-robot control in up to 350 cSt silicone oil with corresponding slowdown in motion speed proportional to the viscosity. The demonstrated range of fluid viscosities from 1’s to 100’s of cSt covers the range of many target application fluids in microfluidics and healthcare such as water (1.0 cSt), cerebral spinal fluid (0.7-1.0 cSt (Bloomfield et al., 1998)), urine (1.0 cSt), blood (3.5 cSt (Stanley A. Berger, 1996)), and the vitreous humour of the eye (700 to several thousand cSt, but non-Newtonian in nature (Lee et al., 1992)).

4.2 Wall Effects

It was suggested in section 2.4 that the presence of a solid boundary near the spinning microrobot could negatively effect the control method by increasing the actual lag angle. The increase in drag torque on a constantly rotating microrobot near a wall is experimentally measured, with results shown in Fig. 14(a). Here, the lag angle is observed using high speed camera as presented in section 3.3, using the top camera to measure the distance between the wall and the microrobot. The corresponding drag torque is calculated from observed lag angles using eq. (22). These results are compared with the theoretical drag torque increase on a sphere, from eq. (26). Both the experimental and theoretical drag torques T_w are normalized by the drag far from the wall (> 5 body lengths), T_d . The experimental results, shown as blue circles in Fig. 14(a) agree well with the theoretical prediction, and

the relatively modest increase in drag torque when operating closer than 1-2 microrobot body-lengths from the wall suggests that the wall effects will only play a minor role in control.

This performance of a microrobot under feedback control in the presence of a wall is tested using a simple path following experiment. Here, a single microrobot is commanded to follow a path 4 mm in length which approached a wall with a variable minimum separation distance δ . The microrobot path error and task completion time are recorded for a number of trials as δ was varied, with results shown in Fig. 14(b). It can be seen that the path error and completion time are negligibly effected for

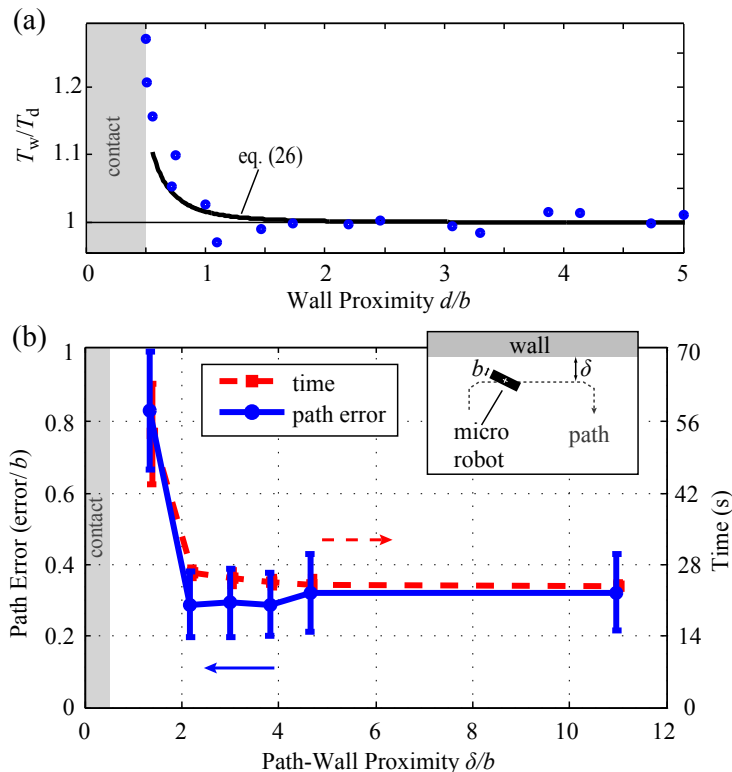


Figure 14: Wall effects for microrobot motion: (a) Effect of wall proximity on the drag torque of microrobot R_7 being pulled slowly towards the wall. The force applied was $0.16 \mu\text{N}$ with a rotation rate of 0.8 Hz and a field strength of 2.0 mT. The axis of rotation was chosen to be perpendicular to the wall to minimize any fluid flow forces. The distances are normalized by the microrobot short axis b , and eq. (26) is presented with the experimental data. (b) Effect of wall proximity on the microrobot path following performance using the position feedback controller. Each data point shows the mean and standard deviation at each wall distance for five samples. Microrobot R_5 follows an x - y path 4 mm in length, as shown in the inset, with varying distance δ from the wall. The rotation rate was 2.0 Hz with a field strength of 1.2 mT, and the fluid is oil with viscosity of 50 cSt. A second ‘virtual’ microrobot was assumed to be holding its position with force $F_2 = [0 \ 0 \ 0]^T \mu\text{N}$. The rotation axis was fixed perpendicular to the wall.

values of d/b greater than 2.0, where b is the microrobot width. When the path approaches within one b distance of the wall, a combination of increased fluid drag torque, possible intermittent wall contact and increased translational fluid drag lead to a significant increase in path error and completion time by a factor of 2-5. From a practical standpoint, it could be sufficient to enforce a minimum wall spacing of $d/b > 2$ to avoid these unpredictable effects. In this case, the effect of nearby walls can be neglected.

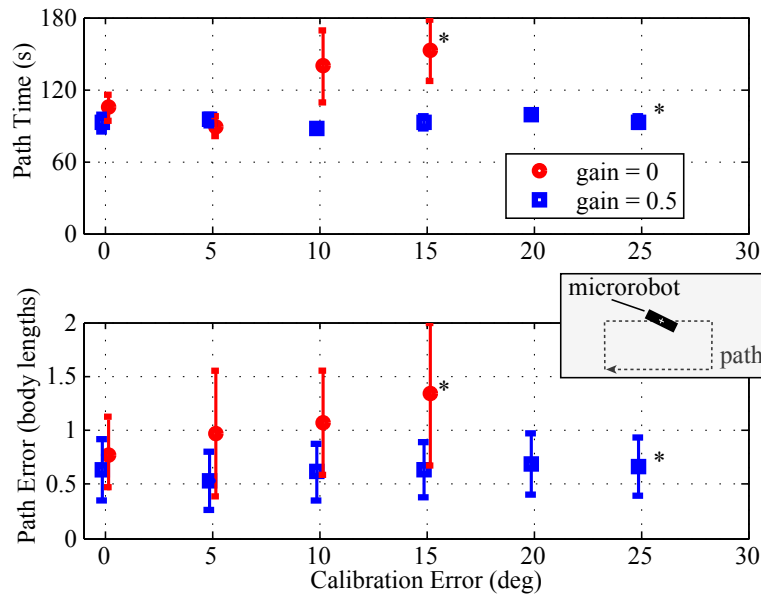


Figure 15: Lag angle feedback control, comparing the case with no velocity feedback (gain = 0) to the feedback case (gain = 0.5) for a single microrobot traversing a rectangular path 2.3 mm wide. Each data point shows the mean and standard deviation at each wall distance for five samples. Data points are shown for each gain to the maximum calibration error tolerable, marked with a ‘*’. Above this calibration error the microrobot does not make progress along the path. Data points are shifted horizontally slightly to aid in visualization.

4.3 Lag Angle Feedback

To test the additional feedback elements discussed in section 2.6, a lag angle feedback term is tested experimentally. Here, the microrobot velocity direction is fed back to the lag angle controller, which forms an updated estimate of the lag angle using eqs. (30-32). This lag angle feedback term has the potential to correct errors in the calibrated lag angle due to miscalibration, wall effects, viscosity change or systematic magnetic coil errors. This controller is tested experimentally, comparing the case with no velocity feedback (gain = 0) to the feedback case (gain = 0.5) for a single microrobot traversing a rectangular path 2.3 mm wide, as shown in Fig. 15. Datapoints are shown for each gain to the maximum calibration error tolerable, marked with a ‘*’. Above this calibration error the microrobot does not make progress along, or diverges from, the path. The calibrated lag angle is 32° , which is used as the ‘ 0° calibration error’ case. A second ‘virtual’ microrobot with zero lag angle has an x -directed force applied at all times to provide a basis for the error calculations. It is seen that the inclusion of the velocity controller significantly reduces the path error, even when the lag angle error is small. It also allows for the system to tolerate larger miscalibrations, increasing from 15° maximum miscalibration for the case with no lag angle feedback to 25° for the case with lag angle feedback. Therefore, the inclusion of lag angle feedback is demonstrated to significantly increase the system tolerance to disturbances in lag angle.

It is possible at close distances for two microrobots to interact with each other by magnetic or fluidic forces. Forces on the microrobot greater than $0.02 \mu\text{N}$, the minimum force required for feedback control, were used to determine the minimum microrobot separation distance allowable. Calculated for R_7 , the magnetic force between two microrobots have an attractive force of $0.02 \mu\text{N}$ at a center to center distance of 1.8 mm but the fluid drag force has the largest impact, extending to a microrobot spacing of 3.4 mm.

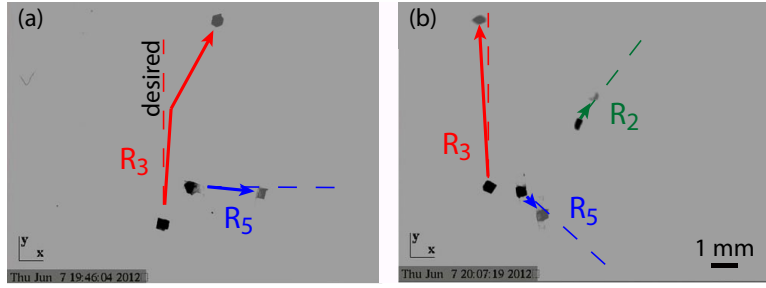


Figure 16: Microrobots controlled using rocking field control, showing desired and actual motion directions in 2D. (a) Two microrobots commanded along perpendicular directions. (b) Three microrobots commanded along different directions. Video available in Extension 1.

The effect of the magnetic torque of one microrobot on another will cause changes in the lag angle and will be a function of the distance between the microrobots and the magnetic field of the coils on the microrobot. The worst-case scenario will be when the field strength of the coil system is on the order of 1 mT and the angle between the microrobot and the field direction is small while the angle between the two microrobots approaches 90° . Under these conditions, the lag angle will experience a 5 percent change 2.6 mm center to center distance between microrobots and a 10 percent change at a 2 mm distance. This shows that to avoid such effects, a minimum inter-robot spacing of several body lengths should be maintained.

4.4 Rocking Applied Field

The final experimental demonstration shows the viability to apply different desired forces on more than two microrobots. Here, the continuous field rotation used previously cannot be used, as it results in a singular \mathbf{A}^* matrix. Therefore, preliminary experimental results for more than two microrobots use the rocking field introduced in section 2.5. Results from this control are shown in Fig. 16 for (a) two and (b) three microrobots moving in independent desired directions in 2D. Here, two microrobots are moved with desired forces of $F_3 = [0 \ 0.01 \ 0]^T \mu\text{N}$ and $F_5 = [0.05 \ 0 \ 0]^T \mu\text{N}$ in Fig. 16(a) and three microrobots with forces $F_3 = [0 \ 0.02 \ 0]^T \mu\text{N}$, $F_5 = [0.02 \ -0.02 \ 0]^T \mu\text{N}$ and $F_2 = [0.01 \ 0.01 \ 0]^T \mu\text{N}$ in Fig. 16(b). No feedback is used in these experiments as a realtime implementation of feedback control is significantly more challenging for the rocking field case due to increase computational requirements. The field strength is 1.2 mT, and is oscillated through $\pm 70^\circ$ at a rate of 18.4 cycles per second, similar to the case shown in Fig. 2. The vertical z -coordinate is not observed during these proof-of-concept demonstrations, but as the microrobots move in the desired directions in the x - y -plane, these results indicate that the actual forces are close to the desired forces. Although it is beyond the scope of this work, with improved magnetic coil strength and microrobot motion tracking, our results suggest that full 3D feedback control of three microrobots could be feasible using this method.

5 Conclusions

We have introduced a method to achieve, for the first time, independent control of multiple microrobots levitating in 3D. We accomplish this through the use of unique heterogeneous microrobot designs, which allow each microrobot to respond differently to the common dynamic driving magnetic fields. The method was analyzed through simulation and experimental results, and shown

to be viable to apply completely independent forces to each microrobot, when averaged over one short field cycle. System parameters were optimized using an analytical model to achieve maximum microrobot forces in the desired directions. Experimental results showed precise path following with two microrobots along arbitrary paths in 3D, and proof-of-concept independent control of three microrobots. The control was demonstrated for a wide range of fluid viscosities of interest in potential microfluidics and medical applications. Visual feedback was used to guide the controller, with additional feedback terms being incorporated to improve performance in the presence of calibration errors or other disturbances such as the presence of nearby walls. However, the presented control method can also be operated in open-loop mode, with reduced motion accuracy. In addition, it was shown theoretically that the control method can be potentially used to independently control any number of microrobots, but with reduction in control authority as the number increases, depending on the strength and precision of the magnetic coil hardware. For the current system hardware, the limit is found to be the full independent control of two microrobots with distinctly different designs, but could potentially be increased through more precise microrobot localization, better field precision and higher magnetic coil strength. Such improvements could also allow for the addressing of very similar microrobot designs.

The multi-robot control scheme introduced in this work could be relevant for many microrobotics applications. A team of microrobots controlled by this method could be independently positioned in inaccessible 3D spaces, for potential use inside microfluidic channels or in the human body for localized therapy or diagnostics. The scheme could be used to extend the effectiveness of existing microrobot techniques for object manipulation and assembly, drug delivery or remote sensing in a distributed manner. Future work will involve improving the system precision and power to enable precise feedback control of more than 2 microrobots in 3D. In addition, the use of microrobot teams for useful tasks in constrained 3D fluidic environments will be explored.

Acknowledgement

The authors would like to thank the NanoRobotics Laboratory members for their support and suggestions, Magnequench, Inc. for supplying magnetic powder and Andrew Gamble and the Carnegie Mellon DSSC for use of magnetometry equipment.

References

- L. Arcese, M. Fruchard, F. Beyeler, A. Ferreira, and B. Nelson. Adaptive backstepping and mems force sensor for an MRI-guided microrobot in the vasculature. In *IEEE International Conference on Intelligent Robots and Systems*, pages 4121–4126, 2011.
- B. Behkam and M. Sitti. Bacterial flagella-based propulsion and on/off motion control of microscale objects. *Applied Physics Letters*, 90:023902, 2007.
- K. Belharet, D. Folio, and A. Ferreira. Three-dimensional controlled motion of a microrobot using magnetic gradients. *Advanced Robotics*, 25(8):1069–1083, 2011.

- I. G. Bloomfield, I. H. Johnston, and L. E. Bilston. Effects of proteins, blood cells and glucose on the viscosity of cerebrospinal fluid. *Pediatric Neurosurgery*, 28(5):246–51, 1998.
- S. Boyd and C. Lemarechal. *Convex Optimization*. Cambridge Univ Press, 2004.
- B. Cullity and C. Graham. *Introduction to Magnetic Materials*. Wiley-IEEE Press, 2008.
- E. Diller, C. Pawashe, S. Floyd, and M. Sitti. Assembly and disassembly of magnetic mobile micro-robots towards deterministic 2-D reconfigurable micro-systems. *International Journal of Robotics Research*, 30(14):1667–1680, 2011a.
- E. Diller, Z. Ye, and M. Sitti. Rotating magnetic micro-robots for versatile non-contact fluidic manipulation of micro-objects. In *IEEE International Conference on Intelligent Robots and Systems*, pages 1291–1296, 2011b.
- E. Diller, S. Floyd, C. Pawashe, and M. Sitti. Control of multiple heterogeneous magnetic microrobots in two dimensions on nonspecialized surfaces. *IEEE Transactions on Robotics*, 28(1):172–182, 2012a.
- E. Diller, S. Miyashit, and M. Sitti. Remotely addressable magnetic composite micropumps. *RSC Advances*, 2(9):3850–3856, 2012b.
- B. Donald, C. Levey, and I. Paprotny. Planar microassembly by parallel actuation of MEMS microrobots. *Journal of Microelectromechanical Systems*, 17(4):789–808, 2008.
- C. Elbuken, M. Khamesee, and M. Yavuz. Design and implementation of a micromanipulation system using a magnetically levitated MEMS robot. *IEEE/ASME Transactions on Mechatronics*, 14(4):434–445, 2009.
- T. W. R. Fountain, P. V. Kailat, and J. J. Abbott. Wireless control of magnetic helical microrobots using a rotating-permanent-magnet manipulator. In *2010 IEEE International Conference on Robotics and Automation*, pages 576–581, 2010.
- D. R. Frutiger, K. Vollmers, B. E. Kratochvil, and B. J. Nelson. Small, fast, and under control: Wireless resonant magnetic micro-agents. *International Journal of Robotics Research*, 29(5):613–636, 2009.
- A. Ghosh and P. Fischer. Controlled propulsion of artificial magnetic nanostructured propellers. *Nano Letters*, 9(6):2243–5, 2009.
- M. Imbaby, K. Jiang, and I. Chang. Net shape fabrication of stainless-steel micro machine components from metallic powder. *Journal of Micromechanics and Microengineering*, 18(11):115018, 2008.
- M. Khamesee, N. Kato, Y. Nomura, and T. Nakamura. Design and control of a microrobotic system using magnetic levitation. *IEEE/ASME Transactions on Mechatronics*, 7(1):1–14, 2002.
- G. Kosa, P. Jakab, F. Jolesz, and N. Hata. Swimming capsule endoscope using static and RF magnetic field of MRI for propulsion. *2008 IEEE International Conference on Robotics and Automation*, pages 2922–2927, 2008.
- M. Kummer, J. Abbott, B. Kratochvil, R. Borer, A. Sengul, and B. Nelson. Octomag: An electromagnetic system for 5-DOF wireless micromanipulation. *IEEE Transactions on Robotics*, 26(6):1006–1017, 2010.

- B. Lee, M. Litt, and G. Buchsbaum. Rheology of the vitreous body. Part I: Viscoelasticity of human vitreous. *Biorheology*, 29(5-6):521–33, 1992.
- Q. Liu and A. Prosperetti. Wall effects on a rotating sphere. *Journal of Fluid Mechanics*, 657:1–21, 2010.
- A. W. Mahoney and J. J. Abbott. Managing magnetic force applied to a magnetic device by a rotating dipole field. *Applied Physics Letters*, 99(13):134103, 2011.
- S. Martel, J.-B. Mathieu, O. Felfoul, A. Chanu, E. Aboussouan, S. Tamaz, P. Pouponneau, L. Yahia, G. Beaudoin, G. Soulez, and M. Mankiewicz. Automatic navigation of an untethered device in the artery of a living animal using a conventional clinical magnetic resonance imaging system. *Applied Physics Letters*, 90(11):114105, 2007.
- S. Martel, M. Mohammadi, O. Felfoul, Z. Lu, and P. Pouponneau. Flagellated magnetotactic bacteria as controlled MRI-trackable propulsion and steering systems for medical nanorobots operating in the human microvasculature. *International Journal of Robotics Research*, 28(571-582), 2009.
- H. Maruyama, T. Fukuda, and F. Arai. Laser manipulation and optical adhesion control of a functional gel-microtool for on-chip cell manipulation. In *IEEE International Conference on Robotics and Systems*, pages 1413–1418, St. Louis, MO, 2009.
- J.-B. Mathieu, G. Beaudoin, and S. Martel. Method of propulsion of a ferromagnetic core in the cardiovascular system through magnetic gradients generated by an MRI system. *IEEE Transactions on Biomedical Engineering*, 53(2):292–299, 2006.
- D. Meeker, E. Maslen, R. Ritter, and F. Creighton. Optimal realization of arbitrary forces in a magnetic stereotaxis system. *IEEE Transactions on Magnetics*, 32(2):320–328, 1996.
- B. J. Nelson, I. K. Kaliakatsos, and J. J. Abbott. Microrobots for minimally invasive medicine. *Annual review of biomedical engineering*, 12:55–85, Aug. 2010.
- C. Pawashe, S. Floyd, and M. Sitti. Multiple magnetic microrobot control using electrostatic anchoring. *Applied Physics Letters*, 94(16):164108, 2009a.
- C. Pawashe, S. Floyd, and M. Sitti. Modeling and experimental characterization of an untethered magnetic micro-robot. *International Journal of Robotics Research*, 28(8):1077–1094, 2009b.
- M. S. Sakar, E. B. Steager, D. H. Kim, A. A. Julius, M. Kim, V. Kumar, and G. J. Pappas. Modeling, control and experimental characterization of microbiorobots. *International Journal of Robotics Research*, 30(6):647–658, 2011.
- M. Sitti. Voyage of the microrobots. *Nature*, 458:1121–1122, 2009.
- A. Solovev, Y. Mei, E. Urena, G. Huang, and O. Schmidt. Catalytic microtubular jet engines self-propelled by accumulated gas bubbles. *Small*, 5:1688–1692, 2009.
- E. R. L. Stanley A. Berger, Werner Goldsmith. *Introduction to Bioengineering*. Oxford University Press, 1996.

- O. Sul, M. Falvo, R. Taylor, S. Washburn, and R. Superfine. Thermally actuated untethered impact-driven locomotive microdevices. *Applied Physics Letters*, 89:203512, 2006.
- S. Tottori, N. Sugita, R. Kometani, S. Ishihara, and M. Mitsuishi. Selective control method for multiple magnetic helical micro-robots. *Journal of Micro-Nano Mechatronics*, 6(3-4):89–95, 2011.
- P. A. Valberg and J. P. Butler. Magnetic particle motions within living cells. Physical theory and techniques. *Biophysical Journal*, 52(4):537–50, 1987.
- P. Vartholomeos, M. R. Akhavan-sharif, and P. E. Dupont. Motion planning for multiple millimeter-scale magnetic capsules in a fluid environment. In *IEEE Int. Conf. Robotics and Automation*, pages 1927–1932, 2012.
- L. Zhang, J. Abbott, L. Dong, B. Kratochvil, D. Bell, and B. Nelson. Artificial bacterial flagella: fabrication and magnetic control. *Applied Physics Letters*, 94:064107, 2009a.
- L. Zhang, J. J. Abbott, L. Dong, K. E. Peyer, B. E. Kratochvil, H. Zhang, C. Bergeles, and B. J. Nelson. Characterizing the swimming properties of artificial bacterial flagella. *Nano Letters*, 9(10):3663–7, 2009b.

Appendix: Index to Multimedia Extensions

The multimedia extensions to this article are at <http://www.ijrr.org>.

Table of Multimedia Extensions

Extension	Type	Description
1	Video	Video showing feedback control of two microrobots, corresponding to Figs. 12 and 13. Also shown in the proof-of-concept application of independent forces to 2 and 3 microrobots using the “rocking” field, corresponding to Fig. 16.